ROYAL SOCIETY
OF CHEMISTRY

PAPER

Check for updates

Self-assembly of polyoxometalate/reduced graphene oxide composites induced by ionic liquids as a high-rate cathode for batteries: "killing two birds with one stone"†

Feng-Cui Shen,[abc] Yi-Rong Wang,[b] Shun-Li Li,[b] Jiang Liu,[b] Long-Zhang Dong, [ID][b] Tao Wei,[b] Yu-Cheng Cui,[b] Xing Long Wu,[d] Yan Xu [ID] *[a] and Ya-Qian Lan [ID] *[b]

The relatively low capacity and poor rate performance of cathodes restrict the development of rechargeable batteries and must be settled urgently due to the ever-growing need of energy storage. Here, we report a new cathode system that produces polyoxometalates (POMs)/ionic liquid (IL)/reduced graphene oxide (RGO) composites, denoted as PIG, by a self-assembly method in which IL plays the role of "killing two birds with one stone". IL not only facilitates the formation of heterogeneous nanocrystalline composites but also acts as the template reagent to feature the morphology of homogeneous nanobelts on the RGO. The PIG system provides us with a theoretical model at the molecular level to give a detailed comparison of a three-dimensional open skeleton formed by different transition metal linkers and a vanadium cage, on the performance of the cathode in batteries. Finally, the targeted composite Mn_3V_{19}-HIL/RGO-1 shows good cycling stability and the best ultrafast rate capabilities (121 mA h g^{-1} at 5000 mA g^{-1} and 73 mA h g^{-1} at 2000 mA g^{-1} for lithium and sodium ion batteries) of POMs-based composites. Furthermore, the PIG system provides a platform for the design of POMs, and even anionic clusters-based composites in the energy conversion and storage, thus giving access to their versatile architectural design and applications.

Introduction

Resource scarcity and environmental degradation have prompted the in-depth study of renewable green energy and highly efficient energy storage systems.[1,2] Rechargeable batteries are the most attractive energy storage and conversion technologies, which can be repetitively charged and discharged to generate a mutual transformation between green electrical and chemical energy.[3,4] Lithium-ion batteries (LIBs) and sodium-ion batteries (SIBs) have dominated the direction of portable electronic devices due to their long cycle life, high energy density, and environmental benignity.[5,6] However, their

practical applications are still hindered by the intrinsically limited choices of cathode materials. Furthermore, the rate capability is a bottleneck for cathode applications due to the required fast charge–discharge rates of Electric Vehicles (EVs) and Hybrid Electric Vehicle (HEVs).[7] Especially for the SIBs, the larger 55% cation radius and higher standard potential suffers from a lower reversible capacity and poor rate capability, so SIB electrodes not simply migrate the excellent host cathodes from those for LIBs.[8,9] Therefore, it is imperative to study alternative cathode materials with high reversible capacity and excellent rate capability for LIBs and SIBs.

At present, extensive studies have been witnessed in traditional transition-metal oxide cathodes,[6,10–12] phosphate cathodes,[13–15] fluorophosphate cathodes,[16–18] *etc.*, for LIBs or SIBs. Especially, nickel-rich layered Ni–Co–Mn cathodes are appealing candidates for a secondary battery because of their high voltage platform and capacity.[19,20] However, high Ni reactivity faces the challenges of intricately structural ordered control synthesis, poor cycling stability and rate capability of cathode, which greatly limits their application.[20,21] Moreover, improving electrode materials and the universality of applications stimulates the pursuit of new potential cathodes.[22,23] Polyoxometalates (POMs), as fascinating metal oxygen clusters, are promising candidates for the self-assembling of functional

[a]College of Chemical Engineering, State Key Laboratory of Materials-Oriented Chemical Engineering, Nanjing Tech University, Nanjing 210009, P. R. China. E-mail: yanxu@njtech.edu.cn

[b]Jiangsu Collaborative Innovation Centre of Biomedical Functional Materials, Jiangsu Key Laboratory of New Power Batteries, College of Chemistry and Materials Science, Nanjing Normal University, Nanjing 210023, P. R. China. E-mail: yqlan@njnu.edu.cn

[c]College of Biological and Chemical Engineering, Anhui Polytechnic University, Wuhu, 241000, P. R. China

[d]National and Local United Engineering Laboratory for Power Batteries, Faculty of Chemistry Northeast Normal University, Changchun, Jilin 130024, P. R. China

† Electronic supplementary information (ESI) available: Detailed characterization, electrochemical performances. See DOI: 10.1039/c7ta09810c

This journal is © The Royal Society of Chemistry 2018

J. Mater. Chem. A, 2018, **6**, 1743–1750 | **1743**

nanocomposites owing to their nanoscale size, multielectron redox behavior, alterable counter cation, and tunable electronic structure.[24–26] POMs have also shown promising cathode activity by providing high capacity for LIBs or SIBs such as $H_3PMo_{12}O_{40}$,[27] $Li_7[V_{15}O_{36}(CO_3)]$,[28] $Na_2H_8MnV_{13}O_{38}$,[29] and $Na_6V_{10}O_{28}$ (ref. 30) which is ascribed to their electronic structures, intrinsic electron-storage capacity, and through shedding light on designs for electrodes. However, there were only a few POMs that have a flexible rate performance. Besides, none of them can be used as applicable cathode material for both LIBs and SIBs. Just as importantly, the good solubility of POMs and poor conductivity are still great challenges for cycle stability with energy storage.[26] A common approach to this dilemma is immobilization of composites on a carbon material support such as carbon nanotubes (CNT)[31–33] or graphene oxide (GO),[34–36] which not only provides larger specific surface areas but also largely improves conductivity of the composites, especially for GO, which has distinct properties such as high mechanical strength and chemical stability favorable for an electrode support. However, negatively charged clusters of POMs are difficult to anchor on negatively charged carbon support GO sheets. Furthermore, the loaded POMs are easily stacked on or peeled off from GO, which inevitably reduces the accessible redox active sites that contact the electrolyte. Therefore, how to design and construct a composite to combine the advantages of POMs and GO is important and challenging.

To address this problem, we selected IL as a positively charged linker to bridge POMs and GO for the following reasons. First, the tunable cluster charge of POMs reacts with IL, resulting in the organic–inorganic POMs–IL heterogeneous composites achieving optimized performance.[37] Second, the simple electrostatic surface immobilization of IL with GO makes it feasible to prepare PIG composites for the cathodes of batteries. Imidazolium-based IL 1-hydroxyethyl-3-methylimidazolium chloride (HIL) was selected to anchor onto GO for its high thermal stability and redox stability. Furthermore, the imidazolium rings can be arranged on the surface plane of GO due to their strong ionic bonding and π–π stacking interaction.[38] Three-dimensional (3D) inorganic open networks constructed via vanadium cages with transition metals Mn, Co, and Fe, such as $[H_6Mn_3V_{18}O_{42}(VO_4)(H_2O)_{12}]\cdot30H_2O$ (Mn_3V_{19}), $[Co_3V_{18}O_{42}(H_2O)_{12}(SO_4)]\cdot24H_2O$ (Co_3V_{18}), and $[Fe_3V_{18}O_{42}(H_2O)_{12}(VO_4)]\cdot24H_2O$ (Fe_3V_{19}), were selected for the cathode, whose 3D framework structures facilitate rapid lithium ion insertion and de-insertion. Furthermore, they provide a theoretical model at the molecular level for a detailed comparison of the effects of different transition metal linkers on the performance of the batteries. After integrating polyoxovandates, HIL and GO, HIL as a "stone to kill two birds" interacts with negatively charged clusters of polyoxovandates through an anion exchange process, forming organic–inorganic crystalline composite POM–IL to avoid the solubility of POMs in the electrolyte. In addition, imidazolium rings are directionally arranged on the surface plane of GO as template agents, resulting in layer-by-layer self-assembly braided nanobelts morphology, which prompts a uniform distribution of POMs molecule clusters on the large surface areas of GO sheets, thus providing a large number of active sites, shorter ions, and electron diffusion pathways. As far as we know, there is no other research involving POMs–IL crystalline composite materials.

The as-prepared PIG composites exhibit superior electrochemical performances. Especially for Mn_3V_{19}-HIL/RGO-1 as LIBs and SIBs, cathodes have high specific capacity and more robust rate performance than other POMs-based cathodes in lithium half-cells. Notably, we have demonstrated for the first time that HIL can be used as template agents to associate with the specified polyoxovandates, guiding the formation of uniform nanobelts morphology. This simple and controllable design can also provide an extensive route for developing versatile electrode materials for energy storage, making a vital step forward with POMs applications.

Results and discussion

The synthesis of composite Mn_3V_{19}-HIL/RGO-1, which was prepared using a one-pot hydrothermal method by mixing Mn_3V_{19} (Fig. S1†), HIL, and GO (3 mg mL^{-1}), is schematically depicted in Fig. 1. Upon hydrothermal treatment at 180 °C for 24 h, the system undergoes immobilization of Mn_3V_{19}, HIL and GO self-assembly from the force of electrostatic interaction, accompanied by reduction of GO to reduced graphene oxide (RGO) by virtue of the action of Mn_3V_{19}. In a control experiment, we synthesized Mn_3V_{19}-HIL/RGO-2 and Mn_3V_{19}-HIL/RGO-3 similarly to Mn_3V_{19}-HIL/RGO-1 with GO loading concentrations of 1 and 5 mg mL^{-1}, respectively. To address the effect of composition on cathode performance, different composites, i.e., Mn_3V_{19}-HIL and Mn_3V_{19}/RGO, were also prepared for comparison. The effect of different ILs on the performance of the LIBs was also investigated by using 1-ethyl-3-methylimidazolium bromide (EIL) as the precursor (labelled as Mn_3V_{19}-EIL/RGO-1). In addition, the influence of polyoxovandates on electrode performance can be tailored by employing $Co_3V_{18}O_{42}(H_2O)_{12}(SO_4)\cdot24H_2O$ (Co_3V_{18}) (Fig. S2†) and $Fe_3V_{18}O_{42}(H_2O)_{12}(VO_4)\cdot24H_2O$ (Fe_3V_{19}) (Fig. S3†) as the precursors denoted as Co_3V_{18}-HIL/RGO and Fe_3V_{19}-HIL/RGO, respectively, by a similar approach to Mn_3V_{19}-HIL/RGO-1.

X-ray diffraction (XRD) was carried out for structural characterization of the composites (Fig. 2a). The diffraction peaks of Mn_3V_{19}/RGO and Mn_3V_{19}-HIL/RGO-1 were indexed as simulated peaks by a single-crystal diffractometer. Their similar diffraction peaks are also presented in the FT-IR spectrum (Fig. S4a†). As shown in the thermogravimetric analysis (TGA) (Fig. S4b†), good thermal stability of Mn_3V_{19}/RGO and Mn_3V_{19}-HIL/RGO-1
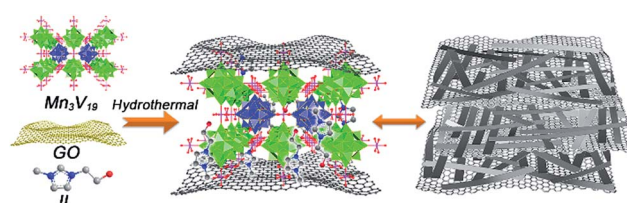

Fig. 1 Schematic illustration of the synthetic process of the composite Mn_3V_{19}-HIL/RGO-1.
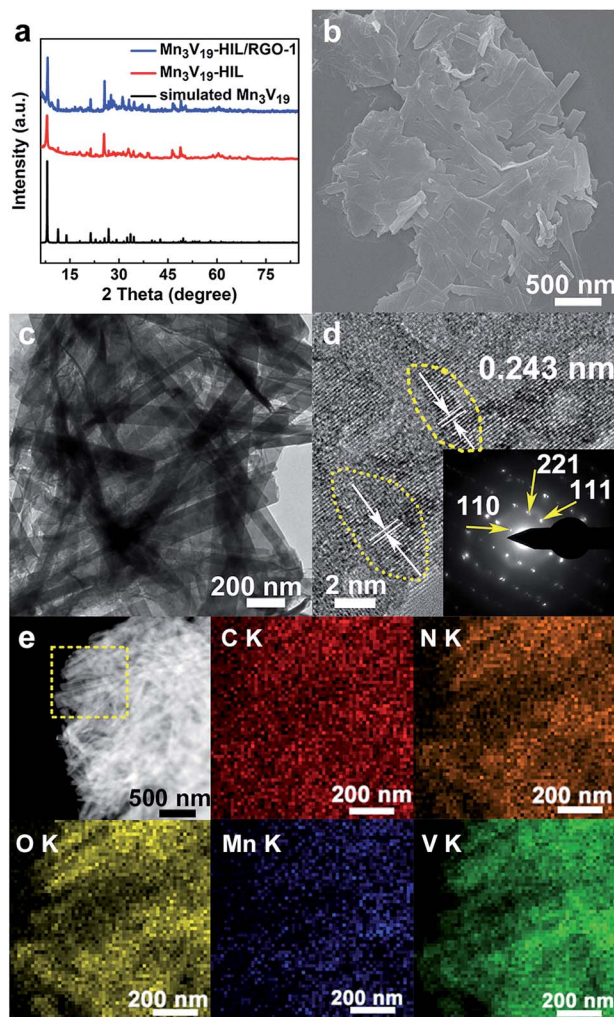
1744 | J. Mater. Chem. A, 2018, **6**, 1743–1750

This journal is © The Royal Society of Chemistry 2018

Fig. 2 Characterization of the Mn_3V_{19}-HIL/RGO-1 and Mn_3V_{19}/RGO composites. (a) XRD patterns of as-prepared samples of Mn_3V_{19}-HIL/RGO-1 and Mn_3V_{19}/RGO. (b) SEM images of Mn_3V_{19}/RGO. (c and d) SEM, TEM image of Mn_3V_{19}-HIL/RGO-1. (e) EDX elemental mapping of C, N, O, Mn, and V in Mn_3V_{19}-HIL/RGO-1.

was obtained. When the temperature was increased to 440 °C, a weight loss of 8% corresponds to the elimination of crystal water and the combustion of reduced graphene oxide in Mn_3V_{19}/RGO-1, while the weight loss of 13% in the composite Mn_3V_{19}-HIL/RGO-1 is attributed to the elimination of crystal water, IL, and the combustion of reduced graphene oxide. The final molar ratio of IL and Mn_3V_{19} (about 1 : 2) was calculated from the weight loss of the composite Mn_3V_{19}-HIL/RGO-1.

The morphology of Mn_3V_{19}-HIL/RGO-1 related samples was investigated by scanning electron microscopy (SEM). An irregular morphology was observed (Fig. S5a and b†) under the absence of HIL with fewer agglomerated Mn_3V_{19} anchoring on the RGO and deciduous POMs. When HIL was drawn into the system, its hydroxyl group interacted with GO, resulting in the imidazolium ring showing a directional arrangement possibility on the surface plane of GO due to strong ionic bonding and π–π stacking interaction. This was accompanied by the GO reducing to reduced graphene oxide (RGO) under the action of

POMs and hydrothermal process. The self-assembly of Mn_3V_{19}, HIL, and GO enables the nanobelt structures to be feasibly assembled into hierarchical RGO (Fig. 2b), causing the larger loading and uniform distribution of Mn_3V_{19} on RGO with a high surface area. However, with the morphologies of Mn_3V_{19}-IL without GO, it can clearly been seen that nanobelts Mn_3V_{19}-IL are stacked together by the influence of van der Waals forces (Fig. S5c and d†). Comparatively, the morphologies of Mn_3V_{19}-EIL/RGO (Fig. S5e and f†) show that irregular nanosheets are distributed on RGO, which may be due to the irregular distribution of EIL. When Co_3V_{18} or Fe_3V_{19} were treated as the precursor of the cathode, then similar nanobelt structures (Fig. S6 and S7†) in Co_3V_{18}-HIL/RGO and Fe_3V_{19}-HIL/RGO were obtained, so we believed that HIL could be a key medium for these nanobelt structures. As shown in Fig. 2c, the transmission electron microscopy (TEM) image of Mn_3V_{19}-HIL/RGO-1 also indicated that a large number of nanobelts Mn_3V_{19}-IL homogeneously wove on the RGO sheets, which afforded massive interpenetrating channels for electrolyte to permeate into the electrode active materials fully and reduce the distance of Li^+ and electron transport simultaneously. Moreover, the clear lattice fringes space of 0.243 nm corresponds to the 443 crystal planes of Mn_3V_{19} (XRD card 89-7670) in the high-resolution TEM (HRTEM) image. Additionally, the interplanar distances of the inset selected area electron diffraction (SAED) with spot patterns in Fig. 2d were calculated manifesting the crystallinity of Mn_3V_{19}-HIL/RGO-1 nanobelts. The uniformity of Mn_3V_{19}-HIL/RGO-1 achieved by the one-pot synthesis method was also verified by EDS elemental mapping, which demonstrates the uniform distribution of C, N, O, Mn, and V throughout the nanosheets (Fig. 2e); this is consistent with energy dispersive X-ray spectrometry (Fig. S8†).

A Raman spectrum of the Mn_3V_{19}-HIL/RGO-1 and Mn_3V_{19}/RGO (Fig. S9†) composites shows similar peaks around 1353 cm^{-1} (D band) and 1593 cm^{-1} (G band), in which the higher area proportion I_D/I_G of Mn_3V_{19}-HIL/RGO-1 indicates RGO with more defects after the integration of HIL.[14,39] Moreover, the N_2 adsorption–desorption isotherm of the as-synthesized composites (Fig. S10a†) was used for Brunauer–Emmett–Teller (BET) surface area analysis (Fig. S10b†). Notably, the specific surface area of Mn_3V_{19}-HIL/RGO-1 was calculated to be 56.65 m^2 g^{-1} by the BET method, which is larger than that of Mn_3V_{19}-HIL (41.87 m^2 g^{-1}) and Mn_3V_{19}/RGO (43.27 m^2 g^{-1}). The large electrochemically active interfacial area of Mn_3V_{19}-HIL/RGO-1 holds great promise for the electrochemical reactions. In addition, a calculation using the Barrett–Joyner–Halenda method indicates that the diameters of mesopores are around 4 nm (Fig. S10b†), facilitating fast lithium-ion diffusion and electrolyte penetration into the electrode.[40]

The chemically lithiated and de-lithiated states of Mn_3V_{19}-HIL/RGO-1 were studied by X-ray photoelectron spectroscopy (XPS) in Fig. S11.† The peaks of the high-resolution C 1s spectrum centered at 284.6 eV, 285.3 eV, and 286.4 eV correspond to the C–C/C=C, C–N, and C–O.[35] The Mn 2p XPS spectrum presents two characteristic peaks at 641.3 and 652.9 eV, attributed to Mn 2p$_{3/2}$ and Mn 2p$_{1/2}$ of Mn^{2+} before and after discharging to 1.5 V.[41] After the de-lithiation process, the V 2p XPS

spectrum displays two peaks of V $2p_{3/2}$ and V $2p_{1/2}$, which can be deconvoluted into 516.7 and 517.6 eV together with 523.5 and 524.8 eV corresponding to V^{4+} and V^{5+} after charging to 3 V.[42] However, V^{3+} peaks displayed at binding energies of 515.8 and 522.9 eV correspond to V $2p_{3/2}$ and V $2p_{1/2}$, because of partial V^{5+} and V^{4+}, reducing to V^{3+} (ref. 42 and 43) after discharging to 1.5 V. The above results revealed that Mn^{2+}, a proportion of V^{5+}, and V^{4+} were reduced to Mn, V^{4+}, and V^{3+}, respectively, in the discharge process.

The electrochemical properties of the Mn_3V_{19}-HIL/RGO-1 cathode were estimated by cyclic voltammetry, first within the voltage range of 1.5–3.5 V *versus* Li/Li$^+$ at a scan rate of 0.2 mV s^{-1} (Fig. 3a), revealing its Li-ion storage electrochemical behavior. The pronounced peaks in the first three consecutive CVs at around the potentials of 2.46 and 2.3 V manifest the lithium ion insertion process corresponding to the partial reduction of V^{5+} and V^{4+} of Mn_3V_{19} to V^{4+} and V^{3+}, while the pronounced peaks at around the potentials of 2.48 and 2.6 V indicate the de-intercalation process due to the re-oxidation of V^{3+} and V^{4+} in transition states of POMs to V^{4+} and V^{5+}. Particularly, there is a small fluctuation of the first CV curve which may be due to some side reactions such as electrolyte oxidation and solid electrolyte interface (SEI) formation, as well as an "activation" process.[44–46] Subsequent CV profiles are almost identical upon further sweeps, suggesting a highly reversible process in the electrochemical reaction. Galvanostatic charge and discharge curves of the Mn_3V_{19}-HIL/RGO-1 electrode for the 1st, 2nd, 10th, and 100th cycles are shown in Fig. 3b at a current density of 100 mA h g^{-1}. The two broad voltage plateaus at approximately 2.65–2.25 V for the discharge process and 2.3–2.6 V for the charging process are in agreement with the CV results, which reveal that part of the capacity for Mn_3V_{19}-HIL/RGO-1 is contributed by the redox reaction of different valence vanadium. Obviously, the gap of the charge–discharge voltage profiles was narrow, implying a low electrode

resistance,[47] which was further confirmed by its electrochemical impedance measurement (EIS) in a frequency range of 0.01 Hz to 100 kHz (Fig. S12†). For comparison, the kinetic properties of Mn_3V_{19}/RGO were also examined. Plots of both samples contain a semicircle in the high to medium frequency range which indicates surface charge transfer resistance between electrode and electrolyte, and a sloped line in the low frequency range assigned to the Li$^+$ diffusion resistance in the composites. Obviously, the charge transfer resistances of Mn_3V_{19}-HIL/RGO-1 composites are lower than those of Mn_3V_{19}/RGO, suggesting that the structure of Mn_3V_{19}-HIL/RGO-1 facilitates electron and Li$^+$ transport.

The cycle performance of Mn_3V_{19}-HIL/RGO-1 (Fig. 3c) shows a good cycling stability at a current density of 100 mA g^{-1}. The initial discharge and charge reversible capacities delivered were 214.2 and 212.9 mA h g^{-1}, with a high coulombic efficiency of 100.6%. Upon 100 cycles of galvanostatic charge–discharge test, the composite shows little capacity fading with reversible discharge and charge capacities of 190.1 mA h g^{-1} and 189.5 mA h g^{-1}, respectively. The stability of the electrode is responsible for the good structural stability for lithium storage in long-term cycling, which can be verified by the SEM images of the Mn_3V_{19}-HIL/RGO-1 electrode after cycling (Fig. S13†). There are almost no changes in the morphology, except for irreversible minor structural defects during cycling. More importantly, the cathode shows a robust rate performance at high current density in Fig. 3d. Reversible capacities of about 210, 175, 162, 156, 152, and 121 mA h g^{-1} were maintained at current densities of 100, 200, 400, 1000, 2000, and 5000 mA g^{-1}, respectively. With the decrease of current density back to 1000 mA g^{-1} and 100 mA g^{-1}, the capacities resumed to the previous values, manifesting good reversibility and excellent rate capability. Cyclic electrode stability of a large current density was further evaluated after 400 cycles at a fairly high current of 5000 mA g^{-1}; it still acquired a high capacity of about 120 mA h g^{-1} (Fig. S14c†).

To gain insight into the relationship between the components and electrochemical performance, other composites, Mn_3V_{19}, Mn_3V_{19}/RGO and Mn_3V_{19}-HIL, were prepared for comparison. Their cycle stabilities and corresponding discharge curves of 100th cycles are evaluated in Fig. S14a and b.† Mn_3V_{19} and Mn_3V_{19}/RGO possess a specific capacity of 33 and 100 mA h g^{-1} with serious decay, while Mn_3V_{19}-HIL exhibits a specific capacity of 40 mA h g^{-1} after 100 consecutive cycles at a current density of 100 mA g^{-1}, thus verifying the importance of HIL and RGO to the cathode performance. Capacity degradation in Mn_3V_{19} and Mn_3V_{19}/RGO is possibly due to dissolution of Mn_3V_{19} in the electrolyte. Furthermore, inhomogeneous distribution of Mn_3V_{19} on RGO without HIL causes dragging of conductivity of the electrode and the transmission of electrons and Li$^+$ ion. Besides, by lacking imidazolium nitrogen atoms, HIL cannot coordinate with lithium, which has adverse effects on electrode electronic properties. Comparatively, Mn_3V_{19}-HIL shows a stable performance exhibiting advantages of organic–inorganic hybrid composites and avoiding the dissolution of Mn_3V_{19}. However, it displays low capacity, due to the packing of an active component with relatively poor conductivity affecting
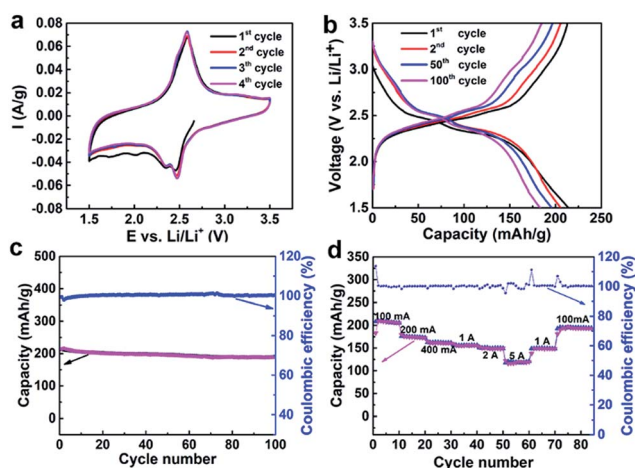

Fig. 3 Electrochemical characterization of Mn_3V_{19}-HIL/RGO-1 as the cathode of LIB in the half cell. (a) Cyclic voltammetry curves of Mn_3V_{19}-HIL/RGO-1 during the first three cycles at a scan rate of 0.2 mV^{-1} in LIBs. (b and c) Discharge–charge curves and cycle-life stability of Mn_3V_{19}-HIL/RGO-1 at 100 mA g^{-1}. (d) Rate capability performance of Mn_3V_{19}-HIL/RGO-1 at various current densities.

1746 | *J. Mater. Chem. A*, 2018, **6**, 1743–1750

This journal is © The Royal Society of Chemistry 2018

electrolyte infiltration and electrons transport. In a control experiment, the effects of GO concentration on the electrochemical performance were investigated as well and are shown in Fig. S14c and d.† Apparently, Mn_3V_{19}-HIL/RGO-2 and Mn_3V_{19}-HIL/RGO-3, representing the concentration of GO 2 and 4 mg mL^{-1}, obtained poor electrode activity. The disappointing performance of Mn_3V_{19}-HIL/RGO-2,3 stresses the key role of GO concentration, which illustrates that a low concentration of GO leads to poor dispersion of Mn_3V_{19}-HIL and poor conductivity. In contrast, when the concentration of GO reaches a certain extent, it may induce stacking and affect the mass of the active composites contacting the electrolyte. To further confirm the contribution of HIL to LIBs, we also researched the performance of Mn_3V_{19}-EIL/RGO (Fig. S15†). It has relatively better stability and recoverable rate performance than Mn_3V_{19}/RGO, indicating the significant role of IL for electrochemical performance. However, the performance of Mn_3V_{19}-EIL/RGO, which is worse than that of Mn_3V_{19}-HIL/RGO-1, is caused by two main reasons. One is the interactions of hydroxyl groups of HIL with Li$^+$ contributing to the capacity of LIBs. Another is that the hydroxyl groups of HIL interact with GO, resulting in the well-proportioned nanobelts structure and facilitating the transport of electrons and ions. In contrast, Mn_3V_{19}-EIL/RGO shows irregular and partially stacked nanosheets morphology, which is inconvenient for an active cathode to contact the electrolyte and may thus affect the electrode performance of the first cycle; this is illustrated in Fig. S15a,† in which only a proportion of V^V is electrochemically reduced to V^{IV}.[28]

This facile self-assembly strategy is, in principle, successfully applicable to synthesizing composites GO with HIL and other polyoxovanadates, which greatly enriches the PIG family. Co_3V_{18} and Fe_3V_{19}, having similar structural units but a different space arrangement with Mn_3V_{19}, were selected for the PIG system. It's worth noting that the PIG cathode composites have similar morphologies when the starting similar structure POMs precursors was applied (Fig. S6 and S7†), illustrating that the HIL template plays the guiding role in the morphology of the composite. Co_3V_{18}-HIL/RGO and Fe_3V_{19}-HIL/RGO composites were utilized for Li-storage electrode materials (see Fig. S16 and S17†) to give a detailed comparison of polyoxovanadates with different transition metal linkers. It can be clearly seen that their capacity only delivered 153 and 107 mA h g^{-1}, respectively, after 100 cycles at a current of 100 mA g^{-1}. Furthermore, when they were tested at a high current density of 5 A g^{-1}, specific capacities of 77.7 and 59.8 mA h g^{-1} were retained. When Co_3V_{18} and Fe_3V_{19} react with HIL, Co^{2+} and Fe^{2+} as their counter cations will be replaced by HIL, which is verified by the EDS data (Table S1†). The atomic ratios of Co to V (8.33%) and Fe to V (10.5%) in as-prepared Co_3V_{18}-HIL/RGO and Fe_3V_{19}-HIL/RGO are lower than that of 17% in Co_3V_{18} and 15.8% in Fe_3V_{19}. The removal of metal ions leads to their relatively low capacity and poor rate performance. Especially for the composite Co_3V_{18}-HIL/RGO, a high proportion of removable Co^{2+} ions and one less vanadium atom in a unimolecule, compared to Mn_3V_{19} and Fe_3V_{19}, may affect its electrochemical performance. While HIL reacts with Mn_3V_{19}, the counter cation H$^+$ will be more favorably replaced than metal ions in the composite Mn_3V_{19}-HIL/RGO-1,

as confirmed by the EDS data. The atomic ratio of Mn to V (14.7%) in composite Mn_3V_{19}-HIL/RGO-1 is close to that of Mn_3V_{19} (15.8%). Thus, the cathode Mn_3V_{19}-HIL/RGO-1 has larger electron acceptance capability and further highlights the virtues of Mn_3V_{19} for energy storage.

As mentioned previously, POMs have flexibly alterable counter cations. Therefore, we attempted to evaluate the electrochemical storage performance of Mn_3V_{19}-HIL/RGO-1 as a conversion cathode for SIBs and obtained the expected performance. Sodium storage behavior was first evaluated by the charge/discharge voltage between 1.5 and 3.5 V versus Na/Na$^+$ at a current of 100 mA g^{-1} in Fig. 4a. In the discharging process, one plateau-like potential region between 1.8–1.5 V can be observed, suggesting two-phase reactions in sodium ion insertion. Meanwhile, the sloping curve manifests a solid-solution behavior between electrode and electrolyte. In the charging process, a charging voltage plateaus was identified which is consistent with the discharging curve. Importantly, the Mn_3V_{19}-HIL/RGO-1 electrode delivered a high initial discharge reversible redox capacity of 160.6 mA h g^{-1} and retained a capacity of 98.2% after 50 cycles at 100 mA g^{-1} (Fig. 4b). Similarly, it also exhibited robust rate performance, delivering 194 mA h g^{-1} at 50 mA g^{-1}, 166 mA h g^{-1} at 100 mA g^{-1}, 140 mA h g^{-1} at 200 mA g^{-1}, 108 mA h g^{-1} at 500 mA g^{-1}, 89 mA h g^{-1} at 1000 mA g^{-1}, and 73 mA h g^{-1} capacity retention even at a high current density at 2000 mA g^{-1} (Fig. 4c). Especially, the capacity at high current densities of 500, 1000, and 2000 mA g^{-1}, as summarized in Table S2,† is superior to other POMs-based catalysts and even comparable to state-of-the-art electrodes.[2,48] Further investigation of cycling stability was conducted at a larger current density of 500 mA g^{-1} in Fig. 4d; the reversible capacity could still reach 92 mA h g^{-1} after 200 successive cycles. To understand the superior rate performances of Mn_3V_{19}-HIL/RGO-1 in SIBs, EIS spectroscopy was investigated for the reaction kinetics in Fig. S18.† It was apparent that the Nyquist plots demonstrated a semicircle at
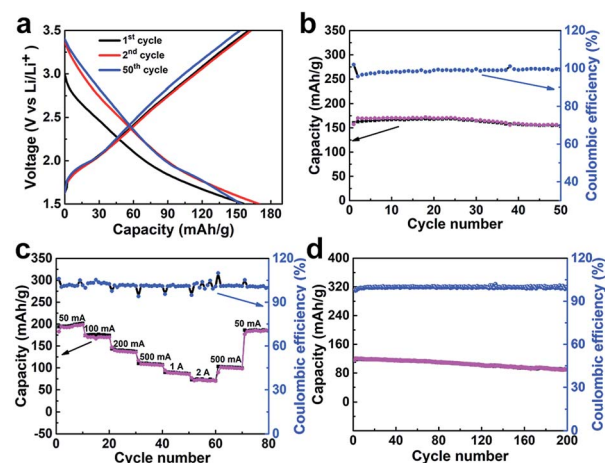
Fig. 4 Electrochemical characterization of Mn_3V_{19}-HIL/RGO-1 as the cathode of SIB in the half cell. (a) Discharge−charge curves and (b) cycle stability of Mn_3V_{19}-HIL/RGO-1 at 100 mA g^{-1}. (c) Rate capability performance of Mn_3V_{19}-HIL/RGO-1 at various current densities. (d) Cycling performance of Mn_3V_{19}-HIL/RGO-1 at 500 mA g^{-1}.
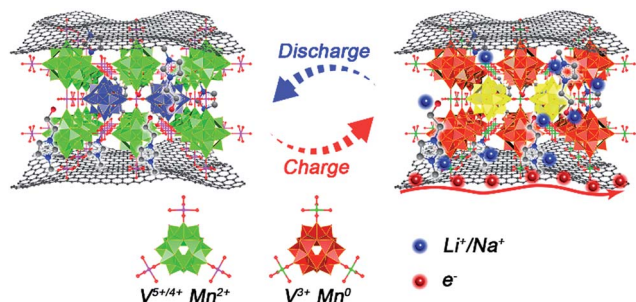
Fig. 5 Schematic illustration of the possible mechanism for the capacity of Mn_3V_{19}-HIL/RGO-1 as the cathode of LIB or SIB.

high to medium frequency regions manifesting a charge-transfer resistance. A small diameter of 109 Ω means a low ion and mass transfer resistance responsible for the excellent rate capability. These outstanding characteristics indeed reveal that Mn_3V_{19}-HIL/RGO-1 is a promising cathode for the SIBs with good cycling stability and high rate capability.

The observed high capacity and favourable robust rate stability are supposed to stem from the intrinsic characters and unique morphology of our cathode. First, the electron sponge Mn_3V_{19} has 40 electrons/ion acceptability at most per molecule due to the formation of highly reduced transition species. Second, polyoxovanadates are more easily dispersed on GO with the aid of HIL, ensuring a larger exposed active surface area and more lithium and sodium storage sites to contact the electrolyte, while the RGO layers structure guarantees the electrons fast transport in the electrode. Third, the nanobelts weaving structure on RGO has good ability to buffer the strain caused by the insertion and extraction of lithium and sodium ions and provides adequate space to accommodate volume expansion of composites during the discharge/charge process. All the factors above contribute to the superior electrochemical performance as the cathode of LIBs and SIBs described in Fig. 5.

Conclusions

In summary, the novel cathode system PIG with uniformly woven nanobelts morphology was synthesized by a facile and environmentally friendly method. A hydrothermal process involves the self-assembly of IL and polyoxovanadates onto the RGO sheets. The ingenious design of applying IL as a positively charged linker plays the role of "killing two birds with one stone" in the PIG system, which is not merely beneficial to form the heterogeneous POMs-IL nanocrystalline composites, but also contributes to the formation of homogeneous nanobelts morphology as well. When the PIG system was utilized as the cathodes of LIBs and SIBs, they exhibited good electrochemical performance. Even more exciting, the Mn_3V_{19}-HIL/RGO-1 shows impressive rate capability superior to other POMs-based composites and most state-of-the-art cathodes (Table S2 and S3†). The cathode combined the advantage of a unique architecture and intrinsic redox properties. In addition, nanobelt composites anchored on a RGO with a large specific surface area and mesoporous structure facilitate the infiltration of

electrolyte, which then greatly accelerates the transport of Li^+ or Na^+ ions and electrons in the electrolyte. Resulting in a superior cathode activity. Furthermore, this IL-assisted strategy addresses the problems of solubility in an electrolyte and poor electronic conductivity of POMs, and sheds light on the great potential of preparing POMs-based composites for energy storage.

Experimental section

Synthesis of Mn_3V_{19}-HIL/RGO-1 nanocomposites and other control samples

Synthesis of $[Co_3V_{18}O_{42}(H_2O)_{12}(SO_4)]\cdot24H_2O$ and $[Fe_3V_{18}-O_{42}(H_2O)_{12}(VO_4)]\cdot24H_2O$.[49] $[Co_3V_{18}O_{42}(H_2O)_{12}(SO_4)]\cdot24H_2O$ was prepared according to a typical synthesis. 0.02 mol of V_2O_5 (3.6376 g) was dissolved in 80 mL of distilled water and heated to 84–86 °C with constant stirring; then 24 mL 0.04 mol $LiOH\cdot H_2O$ (1.6784 g) solution and 0.02 mol $(N_2H_5)_2SO_4$ (2.6024 g) were added to the above solution successively with stirring for 10 min. The mixed solution was diluted to 200 mL and the pH was adjusted to 4.6 with 2 M HCl. Then the solution was reacted for 5 h after adding 0.01 mol of $CoSO_4\cdot7H_2O$ (2.8112 g). The black crystals of $[Co_3V_{18}O_{42}(H_2O)_{12}(SO_4)]\cdot24H_2O$ (signified as Co_3V_{18}) were obtained by vacuum filtration after standing for 12 h. The synthetic procedure for $[Fe_3V_{18}O_{42}(H_2O)_{12}(VO_4)]\cdot 24H_2O$ is similar, using 0.01 mol $FeCl_2\cdot4H_2O$ (1.988 g) instead of $CoSO_4\cdot7H_2O$.

Synthesis of $[H_6Mn_3V_{18}O_{42}(VO_4)\ (H_2O)_{12}]\cdot30H_2O$.[50] In a typical experiment, 3 mL of $LiOH\cdot H_2O$ (5 mmol, 0.2098 g) in solution was added to 10 mL of V_2O_5 (2.5 mmol, 0.4547 g) solution. Then, 2.5 mmol of $(N_2H_5)_2SO_4$ (0.325 g) was added to the mixed solution at 90 °C. After the mixture had been stirred for 10 min, 1.25 mmol of $KMnO_4$ (0.1976 g) was added to the solution, followed by dilution of the mixture to 25 mL. After the mixture had reacted for 1.5 h, the crystals $[H_6Mn_3V_{15}-V_4O_{46}(H_2O)_{12}]\cdot30H_2O$ (signified as Mn_3V_{19}) were obtained by vacuum filtration after standing for 12 h.

Synthesis of Mn_3V_{19}-HIL/RGO-1,2,3 and Mn_3V_{19}-EIL/RGO. GO was prepared following a modified Hummer's method. 30 mg of GO was dissolved in 10 mL of distilled water ultrasonically for 30 min. Then the obtained homogeneous solution was transferred to an autoclave with 0.3 g of Mn_3V_{19} and 0.11 g of 1-hydroxyethyl-3-methylimidazolium chloride (HIL). After sonication for 20 min, the autoclave was transferred to an oven at 180 °C for 24 h. A black sample of Mn_3V_{19}-HIL/RGO-1 was obtained after washing with distilled water and vacuum drying at 60 °C for 12 h. In control experiments, Mn_3V_{19}-IL/RGO-2 and Mn_3V_{19}-IL/RGO-3 were synthesized similarly by altering the GO loading of Mn_3V_{19}-HIL/RGO-1 with 2 mg mL^{-1} and 4 mg mL^{-1}, respectively. Mn_3V_{19}-EIL/RGO was prepared in parallel with Mn_3V_{19}-HIL/RGO-1 using 1-ethyl-3-methylimidazolium bromide (EIL) as the precursor.

Synthesis of Mn_3V_{19}-HIL and Mn_3V_{19}/NRGO. The preparation of Mn_3V_{19}-HIL and Mn_3V_{19}/RGO was also similar to that of Mn_3V_{19}-HIL/RGO-1, but without GO and HIL addition, respectively.

Synthesis of Co_3V_{18}-HIL/RGO and Fe_3V_{19}-HIL/RGO. Co_3V_{18}-HIL/RGO and Fe_3V_{18}-HIL/RGO were prepared as Mn_3V_{19}-HIL/

1748 | J. Mater. Chem. A, 2018, **6**, 1743–1750

This journal is © The Royal Society of Chemistry 2018

RGO-1 employing $Co_3V_{18}O_{42}(H_2O)_{12}(SO_4)\cdot24H_2O$ (Co_3V_{18}), Fe_3-$V_{18}O_{42}(H_2O)_{12}(VO_4)\cdot24H_2O$ (Fe_3V_{19}) as the precursor.

Material characterization

X-ray powder diffraction (XRD) measurements were taken on a D/max 2500 VL/PC diffractometer (Japan) equipped with graphite monochromatized Cu Kα radiation ($\lambda = 1.54060$ Å). Raman measurements were conducted on a Renishaw 1000 Raman spectrometer equipped with a 514.5 nm Ar-ion laser, which was focused on the sample with a 50× objective lens. Thermogravimetric analysis (TGA) was conducted using a Shimadzu-60 thermoanalyzer in air at 10 °C min^{-1} from room temperature to 1100 °C. Nitrogen adsorption–desorption isotherms were characterized at 77 K on a Quantachrome Instruments Autosorb AS-6B. Pore size distributions were measured by the Barrett–Joyner–Halenda (BJH) method. Scanning electron microscopy (SEM) images were recorded by a JSM-7600 F apparatus with an acceleration voltage of 10 kV to examine surface morphology. Transmission electron microscopy (TEM) images were characterized on a JEOL-2100 F instrument with an acceleration voltage of 200 kV. High-resolution TEM (HRTEM) images were performed on a FEI Tecnai G2 F30 instrument with an acceleration voltage of 300 kV with elemental mapping. Energy dispersive X-ray spectroscopy (EDS) and elemental mapping were conducted on a JSM-5160LV-Vantage type energy spectrometer. X-ray photoelectron spectroscopy (XPS) was collected on a scanning X-ray microprobe (PHI 5000 Verasa, ULAC-PHI, Inc.) using Al Kα radiation and the C1s peak at 284.8 eV as an internal standard.

Electrochemical measurements

For LIBs fabrication, preparation of working electrodes was carried out by mixing active material, super-P carbon, and polyvinylidene fluoride (PVDF) in a ratio of 7 : 2 : 1 (weight percent). Then, the slurried were evenly coated on pure Al foil and dried at 90 °C overnight for the night. Coin cells were assembled in 2032-type half cells with Li metal discs and a Celgard 2400 microporous polypropylene membrane as the anode and separator in an argon-filled glovebox whose water and oxygen contents were lower than 1 ppm. The composition of the electrolyte was 1 M LiPF$_6$ in ethylene carbonate (EC)/dimethyl carbonate (DMC)/ethyl methyl carbonate (EMC) in a volume ratio of 1 : 1 : 1. For SIBs fabrication, the preparation of working electrodes was carried by mixing active material, super-P carbon, and carboxymethylcellulose sodium (CMC) in a ratio of 7 : 2 : 1 (weight percent). The fabrication method is similar to that of LIBs except using metallic sodium foil as the counter electrode and 1 M NaClO$_4$ in EC/propylenecarbonate (PC) (1/1 by volume ratio) with 5% fluoroethylene carbonate (FEC) as the electrolyte. Then the electrochemical measurements were executed on a Land Battery Measurement System (Land, CT2001A, China) with a voltage of 1.5–3.5 V at room temperature after the coin cell had been aged for 12 h. Electrochemical impedance spectroscopy (EIS) and cyclic voltammetry (CV) were carried out on a CHI660e electrochemical workstation (Shanghai, China). EIS measurements were estimated in the frequency range of 100 kHz–0.01 Hz with a fixed amplitude of 5 mV at the open-circuit potential. CV curves were recorded at a scan rate of 0.02 mV s^{-1} in the range of 1.5–3.5 V.

Conflicts of interest

The authors declare no competing financial interest.

Acknowledgements

Notes and references

1 B. Dunn, H. Kamath and J.-M. Tarascon, *Science*, 2011, **334**, 928–935.
2 S. Guo, Q. Li, P. Liu, M. Chen and H. Zhou, *Nat. Commun.*, 2017, **8**, 135.
3 M. Winter and R. J. Brodd, *Chem. Rev.*, 2004, **104**, 4245–4269.
4 J. Liu, Y. Wen, Y. Wang, P. A. van Aken, J. Maier and Y. Yu, *Adv. Mater.*, 2014, **26**, 6025–6030.
5 J. B. Goodenough and K.-S. Park, *J. Am. Chem. Soc.*, 2013, **135**, 1167–1176.
6 J. Wang, H. Tang, L. Zhang, H. Ren, R. Yu, Q. Jin, J. Qi, D. Mao, M. Yang, Y. Wang, P. Liu, Y. Zhang, Y. Wen, L. Gu, G. Ma, Z. Su, Z. Tang, H. Zhao and D. Wang, *Nat. Energy*, 2016, **1**, 16050.
7 F. Zou, X. Hu, Z. Li, L. Qie, C. Hu, R. Zeng, Y. Jiang and Y. Huang, *Adv. Mater.*, 2014, **26**, 6622–6628.
8 J. Yang, X. Zhou, D. Wu, X. Zhao and Z. Zhou, *Adv. Mater.*, 2017, **29**, 1604108.
9 Q. Ni, Y. Bai, F. Wu and C. Wu, *Adv. Sci.*, 2017, **4**, 1600275.
10 H.-M. Cheng and F. Li, *Science*, 2017, **356**, 582–583.
11 Y. Zheng, T. Zhou, X. Zhao, W. K. Pang, H. Gao, S. Li, Z. Zhou, H. Liu and Z. Guo, *Adv. Mater.*, 2017, **29**, 1700396.
12 S. Kalluri, M. Yoon, M. Jo, S. Park, S. Myeong, J. Kim, S. X. Dou, Z. Guo and J. Cho, *Adv. Energy Mater.*, 2017, **7**, 1601507.
13 M. Chen, L. Chen, Z. Hu, Q. Liu, B. Zhang, Y. Hu, Q. Gu, J.-L. Wang, L.-Z. Wang, X. Guo, S.-L. Chou and S.-X. Dou, *Adv. Mater.*, 2017, **29**, 1605535.
14 B. Wang, W. Al Abdulla, D. Wang and X. S. Zhao, *Energy Environ. Sci.*, 2015, **8**, 869–875.
15 X. Wang, C. Niu, J. Meng, P. Hu, X. Xu, X. Wei, L. Zhou, K. Zhao, W. Luo, M. Yan and L. Mai, *Adv. Energy Mater.*, 2015, **5**, 1500716.
16 Y. Qi, L. Mu, J. Zhao, Y.-S. Hu, H. Liu and S. Dai, *Angew. Chem., Int. Ed.*, 2015, **54**, 9911–9916.

17 S. T. Dacek, W. D. Richards, D. A. Kitchaev and G. Ceder, *Chem. Mater.*, 2016, **28**, 5450–5460.

18 S. S. Fedotov, N. R. Khasanova, A. S. Samarin, O. A. Drozhzhin, D. Batuk, O. M. Karakulina, J. Hadermann, A. M. Abakumov and E. V. Antipov, *Chem. Mater.*, 2016, **28**, 411–415.

19 H.-J. Noh, S. Youn, C. S. Yoon and Y.-K. Sun, *J. Power Sources*, 2013, **233**, 121–130.

20 D. Wang, R. Kou, Y. Ren, C.-J. Sun, H. Zhao, M.-J. Zhang, Y. Li, A. Huq, J. Y. P. Ko, F. Pan, Y.-K. Sun, Y. Yang, K. Amine, J. Bai, Z. Chen and F. Wang, *Adv. Mater.*, 2017, **29**, 1606715.

21 F. Lin, I. M. Markus, D. Nordlund, T.-C. Weng, M. D. Asta, H. L. Xin and M. M. Doeff, *Nat. Commun.*, 2014, **5**, 3529.

22 N.-S. Choi, Z. Chen, S. A. Freunberger, X. Ji, Y.-K. Sun, K. Amine, G. Yushin, L. F. Nazar, J. Cho and P. G. Bruce, *Angew. Chem., Int. Ed.*, 2012, **51**, 9994–10024.

23 H. Chen and C. P. Grey, *Adv. Mater.*, 2008, **20**, 2206–2210.

24 X. B. Han, Y. G. Li, Z. M. Zhang, H. Q. Tan, Y. Lu and E. B. Wang, *J. Am. Chem. Soc.*, 2015, **137**, 5486–5493.

25 X. Tong, W. Wu, Q. Wu, F. Cao, W. Yan and A. B. Yaroslavtsev, *Mater. Chem. Phys.*, 2013, **143**, 355–359.

26 A. Macdonell, N. A. B. Johnson, A. J. Surman and L. Cronin, *J. Am. Chem. Soc.*, 2015, **137**, 5662–5665.

27 H. Wang, S. Hamanaka, Y. Nishimoto, S. Irle, T. Yokoyama, H. Yoshikawa and K. Awaga, *J. Am. Chem. Soc.*, 2012, **134**, 4918–4924.

28 J. J. Chen, M. D. Symes, S. C. Fan, M. S. Zheng, H. N. Miras, Q. F. Dong and L. Cronin, *Adv. Mater.*, 2015, **27**, 4649–4654.

29 J. Liu, Z. Chen, W. Xuan, S. Chen, B. Zhang, J. Wang, H. Wang, B. Tian, M. Chen, X. Fan, Y. Huang, T. C. Sum, J. Lin and Z. X. Shen, *ACS Nano*, 2017, **11**, 6911–6920.

30 S. Hartung, N. Bucher, H.-Y. Chen, R. Al-Oweini, S. Sreejith, P. Borah, Z. Yanli, U. Kortz, U. Stimming, H. E. Hoster and M. Srinivasan, *J. Power Sources*, 2015, **288**, 270–277.

31 M. Genovese and K. Lian, *ACS Appl. Mater. Interfaces*, 2016, **8**, 19100–19109.

32 D. Gu, W. Li, F. Wang, H. Bongard, B. Spliethoff, W. Schmidt, C. Weidenthaler, Y. Xia, D. Zhao and F. Schüth, *Angew. Chem., Int. Ed.*, 2015, **54**, 7060–7064.

33 W.-J. Yu, L. Zhang, P.-X. Hou, F. Li, C. Liu and H.-M. Cheng, *Adv. Energy Mater.*, 2016, **6**, 1501755.

34 J. S. Li, Y. Wang, C. H. Liu, S. L. Li, Y. G. Wang, L. Z. Dong, Z. H. Dai, Y. F. Li and Y. Q. Lan, *Nat. Commun.*, 2016, **7**, 8.

35 Y. J. Tang, Y. Wang, X. L. Wang, S. L. Li, W. Huang, L. Z. Dong, C. H. Liu, Y. F. Li and Y. Q. Lan, *Adv. Energy Mater.*, 2016, **6**, 7.

36 Y. W. Liu, S. M. Liu, X. Y. Lai, J. Miao, D. F. He, N. Li, F. Luo, Z. Shi and S. X. Liu, *Adv. Funct. Mater.*, 2015, **25**, 4480–4485.

37 S. Herrmann, M. Kostrzewa, A. Wierschem and C. Streb, *Angew. Chem., Int. Ed.*, 2014, **53**, 13596–13599.

38 S. Baldelli, J. Bao, W. Wu and S.-s. Pei, *Chem. Phys. Lett.*, 2011, **516**, 171–173.

39 Y. Zhang, P. Chen, X. Gao, B. Wang, H. Liu, H. Wu, H. Liu and S. Dou, *Adv. Funct. Mater.*, 2016, **26**, 7745.

40 D. Li, D. Yang, X. Yang, Y. Wang, Z. Guo, Y. Xia, S. Sun and S. Guo, *Angew. Chem., Int. Ed.*, 2016, **55**, 15925–15928.

41 T. Yuan, Y. Jiang, W. Sun, B. Xiang, Y. Li, M. Yan, B. Xu and S. Dou, *Adv. Funct. Mater.*, 2016, **26**, 2198–2206.

42 M. Sathiya, A. S. Prakash, K. Ramesha, J. M. Tarascon and A. K. Shukla, *J. Am. Chem. Soc.*, 2011, **133**, 16291–16299.

43 K. Fan, Y. Ji, H. Zou, J. Zhang, B. Zhu, H. Chen, Q. Daniel, Y. Luo, J. Yu and L. Sun, *Angew. Chem., Int. Ed.*, 2017, **56**, 3289–3293.

44 J. Hassoun, K.-S. Lee, Y.-K. Sun and B. Scrosati, *J. Am. Chem. Soc.*, 2011, **133**, 3139–3143.

45 Y. Zhang, C. W. Foster, C. E. Banks, L. Shao, H. Hou, G. Zou, J. Chen, Z. Huang and X. Ji, *Adv. Mater.*, 2016, **28**, 9391–9399.

46 X. Xiong, C. Yang, G. Wang, Y. Lin, X. Ou, J.-H. Wang, B. Zhao, M. Liu, Z. Lin and K. Huang, *Energy Environ. Sci.*, 2017, **10**, 1757–1763.

47 S. W. Oh, S. T. Myung, S. M. Oh, K. H. Oh, K. Amine, B. Scrosati and Y. K. Sun, *Adv. Mater.*, 2010, **22**, 4842–4845.

48 C. Zhu, P. Kopold, P. A. van Aken, J. Maier and Y. Yu, *Adv. Mater.*, 2016, **28**, 2409–2416.

49 M. I. Khan, E. Yohannes and R. J. Doedens, *Angew. Chem., Int. Ed.*, 1999, **9**, 38.

50 M. I. Khan, E. Yohannes and D. Powell, *Inorg. Chem.*, 1999, **38**, 212–213.

1750 | *J. Mater. Chem. A*, 2018, **6**, 1743–1750

This journal is © The Royal Society of Chemistry 2018